Surface photooxidation of polypropylene-based photovoltaic backsheets: A comprehensive spectroscopic investigation

Karissa L. Jensen[a,*], Ashlee Aiello[a], Stefan Mitterhofer[b], Chiara Barretta[c], Gernot Oreski[c], Christopher M. Stafford[d], and Xiaohong Gu[a]

[a] Engineering Laboratory, National Institute of Standards and Technology, Gaithersburg, MD 20899, USA
[b] Foreign Associate, National Institute of Standards and Technology, Gaithersburg, MD 20899, USA
[c] Polymer Competence Center Leoben, Leoben, 8700, Austria
[d] Material Measurement Laboratory, National Institute of Standards and Technology, Gaithersburg, MD 20899, USA

*Corresponding author.
Email address: karissa.jensen@nist.gov
Phone: 301-975-6424

ABSTRACT

The prospect of cost reduction, enhanced performance, and improved sustainability has been driving innovation in the development of new backsheet materials for photovoltaic (PV) modules. Among the materials of interest, polypropylene (PP) has emerged as a promising alternative to fluoropolymer backsheets. As backsheets serve as a barrier providing electrical insulation and protection for the sensitive electrical components of PV modules, comprehensive understanding of the durability of PP-based backsheets is essential to ensure module reliability in the field.

In this study, free-standing coextruded PP backsheets were subjected to artificial weathering to elucidate the degradation behavior. The UV exposure was performed on the NIST Simulated Photodegradation via High Energy Radiant Exposure (SPHERE) under three environmental conditions: 75 °C and 50 % relative humidity (RH), 75 °C and 20 % RH, and 65 °C and 20 % RH. The total UV dose (295 nm to 400 nm) for each film was ≈1710 MJ/m^2, or ≈50 years in Arizona, assuming 10 % albedo. Chemical, optical, and physical changes were monitored throughout exposure. Peak-resolving analysis was applied to attenuated total reflectance-Fourier transform infrared (ATR-FTIR) spectra to obtain functional group concentrations with respect to exposure. The greatest chemical and physical changes are seen after initial exposure (100 MJ/m^2 to 220 MJ/m^2), followed by a saturation point. Spectroscopic results indicate minor accumulation of oxidation products and additive migration. Raman spectroscopy showed a slight increase in crystallinity of the surface layers of the backsheets. Mechanical testing revealed low cracking propensity, with shallow cracks occurring under high strains.

Keywords: FTIR spectroscopy, backsheets, photovoltaics, polypropylene, reliability, polyolefin, photooxidation

1. Introduction

Backsheets are typically thin polymer films found on the back surface of a photovoltaic module, and they serve a critical function as a primary barrier protecting sensitive internal electrical components of the module. This makes them a key element in efforts to lower levelized cost of electricity (LCOE) produced by prolonging installation lifetime [1]. Most importantly, the backsheet also ensures safe operations by providing essential electrical insulation [2]. However, polymers in outdoor installations are susceptible to degradation resulting from a variety of environmental factors, creating potential for photooxidation, thermal oxidation, hydrolysis, and mechanically or electrically induced degradation [1, 3-5]. In PV installations, these degradation processes can lead to discoloration, cracking, delamination, and ultimately, loss of insulation and module failure.

In recent years, a number of factors have been driving the development of backsheets based on polymers such as polypropylene (PP), polyamide (PA), polyethylene terephthalate (PET), and derivatives. Fluoropolymers such as polyvinyl fluoride (PVF) and polyvinylidene fluoride (PVDF) have long been materials of choice for polymeric backsheets, due to their overall resistance to environmental degradation owed to strong carbon-fluorine bonds [1, 2, 6], even though cracking or delamination has also been reported on some PVDF-based backsheets [7, 8]. However, as pressure mounts to lower costs of PV materials, the high price of fluoropolymers has been inciting interest in fluoropolymer-free alternatives. Backsheets produced via coextrusion, such as those based on PA, PP, and PET, enable one-step manufacturing and lower the LCOE compared to laminated, multi-layer, fluoropolymer backsheets. Coextruded backsheets also require no adhesive, which reduces the risk of delamination in the field [9]. Notably, improvement of coextruded backsheets also allows for performance optimization through the tuning of material properties, such as reflectivity, permeability, and thermal conductivity [10-13]. Finally,

fluoropolymers cannot be recycled via conventional methods and generate harmful byproducts on incineration [12, 14]. These end-of-life challenges are at odds with the guiding principles at the heart of renewable energy generation [15]. Eliminating the fluoropolymer layer reduces environmental harm by enhancing recyclability of these emerging backsheets [16].

Despite the growing demand in the PV industry for more economical alternatives, there is a collective apprehension surrounding coextruded backsheets in the wake of the disastrous failure of widely deployed polyamide backsheets. The emergence of polyamide backsheet cracking after only 4-7 years in the field, which was not detected by reliability testing, stirred alarm within the PV industry and led to extensive scrutiny of both the material itself and the existing standard test methods [17-21]. However, this ordeal has been accompanied by a great deal of new knowledge. Importantly, the lessons learned from the polyamide failure underscore the necessity for detailed investigation of the degradation mechanisms of all components of new proposed PV packaging. Furthermore, insight into the failure of these backsheets has improved understanding of what may make a viable coextruded backsheet, as well as how to better detect insufficiencies. This progress is demonstrated in the research and development of combined accelerated stress testing (C-AST) in recent years, as well as sequential testing and solder bump testing, which have each been successful in identifying failure modes in polyamide backsheets that conventional accelerated stress tests had failed to predict [19, 22-26]. This wealth of new research serves as a great asset in the continued effort towards innovation in fluoropolymer alternatives.

Recently, backsheets based on polypropylene (PP) have emerged as a novel and appealing candidate for replacement of more expensive PET- and fluoropolymer-based backsheets [11, 12, 26, 27]. As PP is a well-established and widely used commercial and consumer polymer, there is a variety of existing literature on the degradation of PP [28-35], which serves as an excellent foundation for further investigation.

Research on PP as a material of interest for PV backsheets, however, is still emerging. Modified PP-based backsheets have been found to show low cracking propensity, with degradation confined to the surface layer, using solder bump coupons subjected to sequential accelerated stress testing [26]. Recent work shows selective permeability of PP backsheets, allowing escape of acetic acid, an undesirable and damaging degradation product of the common encapsulant ethyl vinyl acetate (EVA), while maintaining protection against atmospheric water vapor [12]. The oxygen transmission rates (OTR) for PP-based backsheets is also higher than for standard PET-core backsheets [12]. Moreover, the functionalized properties of PP, such as the selective permeability, as well as higher reflectance, have been shown to increase performance and stability of tested PV modules [11]. These results, in addition to the lower cost of production and improved recyclability of PP, create considerable interest in the continued development of PP as a functional, reliable, sustainable, and affordable backsheet material.

However, some studies have shown PP to have relatively poor UV durability [31]. There also remains limited published material investigating the photo-oxidative degradation of PP backsheets in depth, specifically in service conditions expected for PV backsheets. Therefore, there remains a significant need for research on the UV stability of PP backsheets under service conditions. In particular, a research gap persists for the study of PP materials specifically prepared for PV service. These preparations are expected to contain UV stabilizers, which will, of course, have a significant influence on the UV performance of the materials.

Oxidation in PP has been previously shown to be most severe in surface layers [12, 26]. Results from Carlsson and Wiles have also shown ATR spectroscopy to be a useful test for identifying the onset of photooxidation in unstabilized PP [36]. Previous spatially resolved studies on UV degradation on PV

polymeric backsheets have shown depth-dependent degradation consistent with UV attenuation and limited oxygen diffusion [37-39]. Furthermore, bulk damage in backsheets has generally been considered to be facilitated by surface degradation [27]. Surface investigation therefore offers an excellent environment for reliable quantification of oxidation and serves as an early indicator for continued degradation, while allowing utilization of non-destructive methods of analysis. For this reason, the current study is focused on presenting a comprehensive investigation of the surface degradation of PP-based PV backsheets exposed to UV weathering. Please note that a concurrent study on this system, presenting a spatially resolved evaluation of the backsheet degradation utilizing Raman spectroscopy, is forthcoming [40].

Free-standing coextruded PP backsheets were subjected to artificial weathering under different conditions to further elucidate the degradation behavior of this material in various environmental conditions: 65 °C/20 % relatively humidity (RH), 75 °C/20 % RH, and 75 °C/50 % RH. These backsheets were examined using a variety of spectroscopic, optical, and mechanical test methods. Different oxidative degradation products were distinguished using FTIR peak-resolving technique, allowing for a quantitative examination of the evolution of degradation products. Additionally, the fragmentation testing presented here allows for the simulation of stress in a controlled, quantitative manner [41], enabling connection of spectroscopic results to mechanical consequences. By bridging the quantitative analysis of the chemical, optical, and mechanical effects of oxidative degradation, this study provides an improved understanding of the long-term UV durability of PP backsheets.

2. Experimental

2.1. Materials

This study examined pristine, free-standing, coextruded backsheets based on a PP block copolymer modified with a low amount of polyethylene (PE) [11, 12]. Based on cross-sectional measurement by laser scanning confocal microscopy, the backsheets comprise three coextruded layers (Fig. 1): a 27.7 µm ± 0.4 µm PP air side (outer) layer, a 224 µm ± 8.8 µm PP core, and a 26.5 µm ± 2.8 µm PP cell side (inner) layer, in agreement with previous published dimensions of this material [11]. The air and cell layers are pigmented with TiO_2, and Raman microscopy and XPS analysis indicates possible additional mineral fillers, such as calcium carbonate ($CaCO_3$). More discussion of the XPS results may be found in Section 3.3. No adhesives were found in the backsheets.

The findings presented in this paper are representative of the specific investigated backsheets described. The exact UV stabilizers and fillers used are proprietary and details are not available at this time; however, the UV aging of backsheets is strongly influenced by this system of additives. This should be considered when evaluating the results of any weathering experiment on emerging materials.

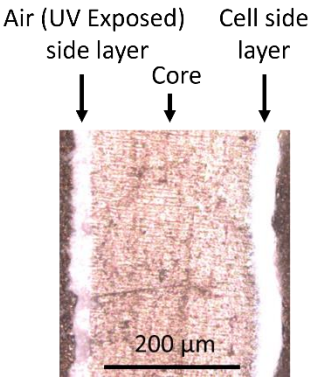

Fig. 1. Optical microscope image of cross section of PP-based backsheet. Dark regions on edges are potting material (epoxy). The cell side layer is visibly rough compared to the air side layer. In this image, roughness of the air side layer is exaggerated by the roughness of the diamond saw used to cut the sample.

2.2. Accelerated laboratory weathering

Three PP backsheet samples were subjected to accelerated weathering using the NIST SPHERE (Simulated Photodegradation via High Energy Radiant Exposure) [42] under an averaged ultraviolet (UV) irradiance of approximately 135 W/m^2 (295 nm to 400 nm). Bearing in mind the Department of Energy (DOE) target of 50-year modules, the total UV dose (295 nm to 400 nm) for each film was approximately 1710 MJ/m^2, equivalent to approximately 50 years in Arizona, assuming 10 % albedo [43]. Samples were weathered at 65 °C and 20 % RH, 75 °C and 20 % RH, and 75 °C and 50 % RH, with one backsheet at each set of conditions. Conditions were selected according to condition A3 of IEC 62788-2 [44], and temperature and humidity were varied independently to investigate the effect of each on the degradation. Each sample was mounted on a black anodized sample holder with an anodized aluminum backing plate, with the air side of the backsheet exposed to UV (see Fig. S1). Backsheets were removed at planned intervals for nondestructive chemical, optical, and morphological testing. Additionally, a piece of each sample was cut and removed for mechanical testing, XPS measurement, and Raman measurement at 3 different doses, spread out over the course of the experiment (approximately 340 MJ/m^2, 1110 MJ/m^2, and 1710 MJ/m^2).

2.3. Attenuated total reflectance Fourier-transform spectroscopy (ATR-FTIR)

In this study, a Nicolet iS50 FT-IR (Thermo Fisher Scientific, Madison, WI) with a diamond ATR accessory was used to characterize the chemical degradation of the backsheets on the air side (exposed to UV) and the cell side (not exposed to UV). The instrument is equipped with a deuterated, L-alanine doped triglyceride sulfate (DLaTGS) detector at room temperature and a potassium bromide (KBr) beamsplitter. Spectra were collected in the range of 4000 cm^{-1} to 350 cm^{-1}, averaging 128 scans collected at a resolution of 4 cm^{-1}with dry air as a purge gas. When necessary, FTIR spectra were corrected for atmospheric water vapor using an existing Python 3 program utilizing a least squares approach, modified to allow minor adjustments [45]. All ATR-FTIR spectra were processed and analyzed using OriginPro 2020 [46], including baseline correction and peak deconvolution, normalizing to 2722 cm^{-1}, which has been suggested to be associated with CH_3 vibrations of PP [31, 35].

2.4. Yellow index (YI) measurement

Colorimetry was used to characterize the optical changes of the backsheets with degradation. Yellow index measurements were obtained using a BYK Spectro-Guide Sphere Gloss handheld color meter (product number 6834) (BYK-Gardner GmbH, Geretsried, Germany), with d8 geometry and 60° gloss

measurement. Five measurements were taken on each side of each backsheet sample, and an average was computed. Delta YI (ΔYI) is used to report the change in YI from initial measurement.

2.5. Laser scanning confocal microscopy (LSCM)

A Zeiss model LSM800 (Carl Zeiss Microscopy, White Plains, NY) LSCM was used to image the surface of the backsheets over the course of exposure. Objectives of 5× (z-step of 10.00 µm) and 50× (z-step of 1.00 µm) were used to capture images in reflection mode with a laser wavelength of 405 nm. Two-dimensional images presented in this study are orthogonal projections of 3-dimensional z-stacks in the X-Y plane generated by ZEN (Lite) [47] software using a maximum intensity projection method. Images acquired using the 5x objective are 2.56 mm square, and images acquired using 50× are 255.56 µm square. All images consist of 1024 × 1024 pixels unless otherwise noted.

To obtain roughness data, topology data was exported to ConfoMap ST [48]. Confomap was used to remove the macro-scale form variation using a degree 3 polynomial form. A standard, robust Gaussian filter was applied to the data with a cut-off of 200 µm. The root-mean-square height of the surface was calculated, as a quantifier of surface roughness.

2.6. Fragmentation testing

To evaluate crack propensity, samples were cut into 5 mm wide strips for fragmentation testing, mounted on a mini tensile tester under a LSCM (a Zeiss model LSCM 800, described above), and imaged using a 50× objective (see Fig. S2 for experimental setup). Uniaxial strain was applied to each sample in planned increments, increasing from 0.1 % to 20 %, and images were obtained at each interval. The images were collected as three 238 µm squares and combined to form a composite image having the dimensions 715 µm wide × 238 µm high. ConfoMap ST was used to remove the larger surface form using a degree 5 polynomial form, and a line profile was extracted from the sample images to examine cracking depth. This fragmentation method is described in detail by Mitterhofer, *et al*., and was shown to be capable of recreating backsheet cracking in a coextruded PA backsheet and a 7-layer laminated backsheet comprising PET outer and core layers, adhesive, and EVA inner layer (PPE) in controlled conditions [41].

2.7. X-ray photoelectron spectroscopy (XPS)

Surface elemental analysis of the backsheets was conducted by XPS (AXIS Ultra DLD Spectrometer, Kratos Analytical). XPS measurements were performed using a monochromatic Al K_α source (1486.6 eV) operating at 140 W. The base pressure of the sample analysis chamber was $\approx 1.33 \times 10^{7}$ Pa (or 1.0×10^{9} Torr), and spectra were collected from a nominal spot size of 300 µm × 700 µm. Measurements were performed in hybrid mode using electrostatic and magnetic lenses, and the pass energy of the analyzer was set at 160 eV for survey scans and 20 eV for high resolutions scans, with energy resolutions of 0.5 eV and 0.1 eV, respectively. Charge neutralization was achieved using a low energy electron flood gun, and all spectra were shifted with respect to the C-C peak in the C 1s envelop to be 285 eV. Three measurements were taken for each sample. All XPS data analysis was completed using CasaXPS software package.

2.8. Raman spectroscopy

Raman spectroscopy measurements were performed using a Senterra II confocal Raman microscope (Bruker, Ettlingen, Germany) with a 785 nm excitation wavelength at 25 mW focused through a 10× objective using a 50 µm × 1000 µm aperture into the sample. Four 15 s exposures were averaged together to generate the spectrum. Five spots were measured for each sample side. Background subtraction was completed using Opus software package.

2.9. Nanoindentation

Nano-indentation was conducted to investigate the changes of Young's modulus (E) of the sample surface using a G200 nano-indenter (KLA, Milpitas, CA). A 2 μm, 90° sphero-conical diamond indenter tip was indented to a depth of 3 μm using the continuous stiffness method [49]. E was extracted from the flat areas of the depth-modulus curves of 50 indents in each sample using a custom filtering algorithm [50].

3. Results

3.1. FTIR spectra indicate moderate degradation of polypropylene

ATR-FTIR serves as a nondestructive means for evaluating chemical degradation of polymeric backsheets during accelerated laboratory weathering. In the case of PP, the FTIR spectrum is well documented. Peak assignments for PP from the literature are reported in Table 1. The peak at 1375 cm^{-1} (associated with symmetric in-plane bending of CH_3 in PP) was used for normalization of FTIR data [51-53]. ATIR-FTIR results show extremely minor changes in intensity of characteristic polypropylene peaks over the course of exposure, suggesting very little degradation of the polymer (Fig. 2).

Table 1 FTIR and Raman peak assignments for PP backsheets.

Frequency (cm^{-1}) FTIR	Raman	Polymer	Assignment	Ref.
2960, 2949	2955	PP	Asymmetric stretching (ν_{as} -CH_3)	[51, 53-55]
2916	n/a	PP and PE	Asymmetric stretching (ν_{as} -CH_2)	[51-54, 56]
2878, 2866	n/a	PP	Symmetric stretching (ν_s -CH_3)	[51, 53, 54, 57, 58]
2849	2885, 2844	PP and PE	Symmetric stretching (ν_s -CH_2)	[51, 52, 57-59]
2838	n/a	PP	Symmetric stretching (ν_s -CH_2)	[51, 53, 56]
2722	n/a	PP	ν CH_3^*	[31, 35]
1471, 1462		PE	Asymmetric in-plane bending ($\delta_{as,\ in\text{-}plane}$ -CH_2)	[51, 52, 57]
1457	1460, 1439	PP	Asymmetric in-plane bending ($\delta_{as,\ in\text{-}plane}$ -CH_2)	[51, 55, 59]
1436	n/a	PP	Asymmetric in-plane bending ($\delta_{as,\ in\text{-}plane}$ -CH_3)	[51, 55]
1375	n/a	PP and PE	Symmetric in-plane bending ($\delta_{s,\ in\text{-}plane}$ -CH_3)	[51-53]
	1361	PP	Wagging (ω -CH_3)	[60]
1359	1359	PP	Symmetric in-plane bending ($\delta_{s,\ in\text{-}plane}$ -CH_2)	[51, 57]
1305	1331	PP	Wagging (ω -CH_2) + twisting (τ CH_2)	[54, 58]
n/a	1299	PE	Wagging (ω -CH_2) + bending (δ – CH)	[58]
n/a	1221	PP	Twisting (τ -CH_2) + wagging (ω -CH) + stretching (ν C-C $_{polymer\ backbone}$)	[55]
1167	1169	PP	Rocking (ρ -CH_3) + stretching (ν C-C)	[51, 54, 55]
n/a	1154	PP	Stretching (ν C-C $_{polymer\ backbone}$) + bending (δ – CH)	[55]
998	n/a	PP	Rocking (ρ -CH_3) + wagging (ω -CH_2) + bending (δ – CH)	[32, 51, 54, 55]
974	975	PP	Stretching (ν C-C $_{polymer\ backbone}$) + Rocking (ρ -CH_3)	[32, 51, 54, 55, 61]

898	n/a	PP	Rocking (ρ -CH_2)	[51]
841	842	PP	Rocking (ρ -CH_2)	[35, 51, 55]
809	810	PP	Stretching (ν C-C $_{\text{polymer backbone}}$)	[51, 54, 55]
n/a	611	n/a	Rutile TiO_2 (A_{1g})	[62, 63]
n/a	450	n/a	Rutile TiO_2 (E_g)	[62, 63]

*There is some literature disagreement on the exact nature of the vibrations contributing to the peak at 2722 cm^{-1}; however, there is general consensus they arise from the CH_3 group.

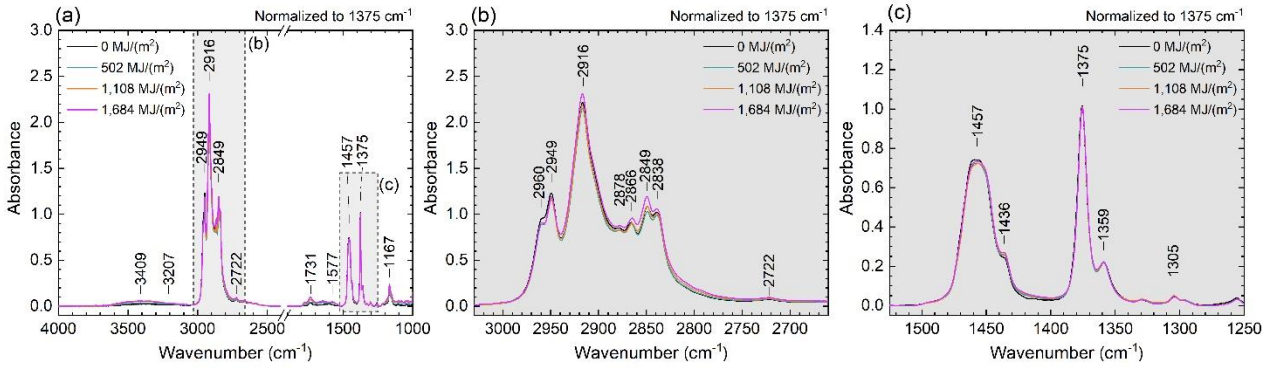

Fig. 2. (a) Full FTIR spectra (4000 cm^{-1} to 1000 cm^{-1}) of UV-exposed side (air side) of PP-based backsheets weathered at 75 °C and 20 % RH, over the course of exposure; (b) expansion of spectra from 3030 cm^{-1} to 2660 cm^{-1} and (c) 1525 cm^{-1} to 1250 cm^{-1} showing gradual decrease in characteristic PP peaks as total UV dose increases. Refer to Fig. S3 and Fig. S4 for corresponding FTIR spectra of samples exposed at 65 °C/20 % RH and 75 °C/50 % RH, as well as Fig. S5, Fig. S6, and Fig. S7 for FTIR spectra of cell side surface.

Oxidative degradation of PP is understood to result in the formation of various carbonyl products, which appear in the FTIR spectral region of approximately 1800 cm^{-1} to 1700 cm^{-1} [31-33], as well as hydroxyl products (3600 cm^{-1} to 3200 cm^{-1}), vinyl (1660 cm^{-1} to 1630 cm^{-1} and 909 cm^{-1}) [32, 64], and vinylidene (1660 cm^{-1} to 1630 cm^{-1} and 888 cm^{-1}) [32, 64]. Numerous peaks in agreement with these previous results are present in the spectra of the aged backsheets (see Table 2). Due to the copolymer nature of the backsheets, some oxidative product peaks typically associated with the photooxidation of PE are present, as well [65, 66]. Finally, a pair of sharp peaks at 1577 cm^{-1} and 1543 cm^{-1} are visible in the aged samples, attributable to the additive calcium stearate ($CaSt_2$) [67].

The intensity of the oxidation product peaks remains relatively low throughout the course of the exposure, with the highest intensity peak in the carbonyl region (1737 cm^{-1}, assigned to ester products) reaching a maximum normalized intensity of 0.1, less than 5 % the normalized intensity of the strongest characteristic polypropylene peak present, 2.31 (2916 cm^{-1}) (Fig. 2). These results, together with the moderate decrease of characteristic polypropylene peaks, suggest relatively minor oxidative degradation of the PP with weathering. Please be aware these results are specific to the emerging PP-based backsheet investigated in this study.

3.2. Oxidation product formation

3.2.1. FTIR peak resolving analysis of oxidative product regions

Oxidative degradation of PP is known to proceed via a free radical chain oxidation mechanism resulting in hydroperoxides and ketones. Ketones generated may further degrade through Norrish type I and II reactions resulting in various oxidative products, including lactones, esters, ketones, carboxylic acids, vinyl, and vinylidenes (see discussion in Section 3.2.6) [31-33, 64]. This process is known to take place preferentially on the surface of PP, and ATR has previously been identified as a useful tool for identifying

the onset of PP oxidation [36]. In an effort to monitor the evolution of the oxidative degradation products of the backsheets, peak deconvolution was undertaken in the region of 1820 cm^{-1} to 1520 cm^{-1}. A complete description of the peak identification and deconvolution process may be found in Section S2.2. The results are consistent with previous studies on outdoor-exposed PP [31-33]. To eliminate the need for C=C peaks differentiation, a similar peak-finding and deconvolution procedure was applied in the region of 920 cm^{-1} to 860 cm^{-1} to examine bands associated with C-H wags of vinyl and vinylidene groups. All degradation product peak assignments were made based on existing PP and PE degradation literature [31-33, 65, 66], as well as FTIR spectral analysis [53, 64], and are summarized in Table 2. An example deconvolution is shown in Fig. 3.

Table 2 FTIR absorbance regions for oxidative degradation products of PP and PE; Ref. [31-33, 64]

Absorbance Region (cm^{-1})	Band Frequency (cm^{-1})	Degradation Products Group	Vibration
1785 to 1763	1783, 1773, 1764	Lactones	C=O stretch
1750 to 1726	1749, 1742, 1735, 1727	Esters	C=O stretch
1724 to 1714	1721, 1715	Ketones	C=O stretch
1713 to 1705	1711, 1705	Carboxylic Acids	C=O stretch
917 to 905	917, 909	Vinyl	C-H wag
895 to 885	892, 886	Vinylidene	C-H wag

The indices of the different carbonyl products were obtained by dividing the areas of peaks associated with particular products by the area of the peak at 1375 cm^{-1}, then summing the resulting values for peaks of the same product functional group. This was repeated for each product functional group, for each measurement. Very small peaks are present in the oxidative product region on the unexposed backsheets. This may be due to a small amount of thermal oxidation occurring during manufacture [36, 68]. To examine product trends over the course of exposure, the calculated product indices are subtracted from the initial values to account for this and isolate new degradation.

$$Product\ Group\ Index = \sum_{n=1}^{k} \frac{A_{product\ peak\ n}}{A_{1375\ cm^{-1}}}\ ;$$

$$k = number\ of\ product\ group\ peaks$$

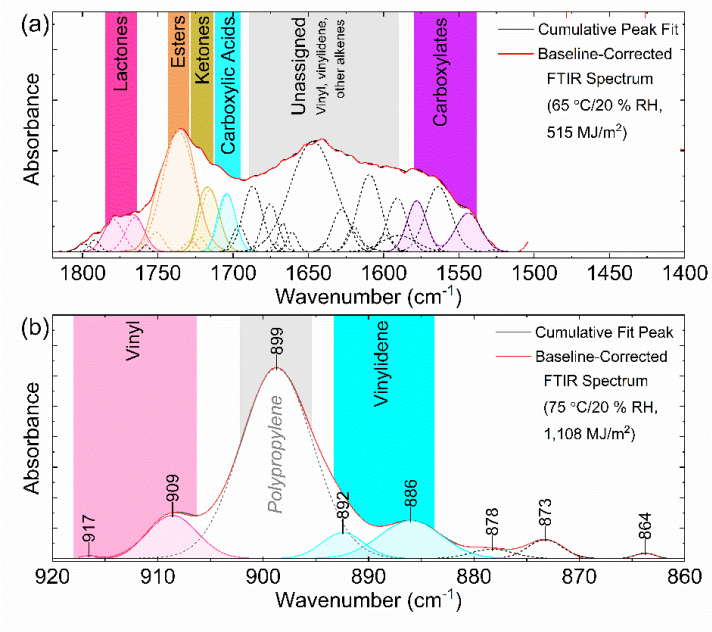

Fig. 3. FTIR spectrum expansions showing (a) example deconvolution results of product peaks associated with oxidative degradation, as well as carboxylate peaks (associated with polymer manufacturing lubricant), in the region of 1850 cm^{-1} to 1400 cm^{-1}, and (b) example deconvolution results of product peaks associated with vinyl and vinylidene degradation products, in the region of 920 cm^{-1} to 860 cm^{-1}. Shaded areas with solid lines represent the regions of product peaks of the same type for which peak areas were summed; dotted, colored lines are the component fit peaks of those regions; and black dotted lines are those peaks which were fit but excluded from the analysis (not a peak of interest for this study).

3.2.2. UV irradiation effect on oxidation product formation

Peak-resolving analysis of the oxidation product region revealed a distinct shift in oxidative degradation product trends after an initial period of exposure. Nearly all oxidative product groups show an initial sharp increase, followed by a leveling-off behavior, indicating a saturation point of these degradation products after an initial exposure period. This observation agrees with previous PP aging studies observing a saturation point of oxidation degradation products [28, 29, 69]. For carbonyl, this change in slope is seen at or around the measurements conducted after 640 MJ/m^2 exposure (shaded in Fig. 4, Fig. 5, and Fig. 6). For some products, the quantity is seen to gradually decrease after reaching a maximum, rather than completely stagnate.

The present study shows significantly greater accumulation of carbonyl products on the side of the backsheet receiving UV exposure (air side). On the UV-exposed side, esters, lactones, carboxylic acids, and ketones are observed, showing a steep increase in concentration followed by a plateau, as discussed. The slight loss of carboxylic acids over time may be attributed to loss of volatile, low-molecular weight acids (such as acetic acid) [12, 69].

Carbonyl product formation on the cell (dark) side of the backsheets is dominated by carboxylic acid and ketones formation. These products follow a similar, though not identical, trend to the UV-exposed side, though the total amounts are considerably lower, and the differentiation is not as clear as for lactones and esters. However, esters and lactones show little change on the side not exposed to UV, seen in Fig. 4 (a) and (c), indicating the formation of lactones and esters depends more heavily on the presence of UV light.

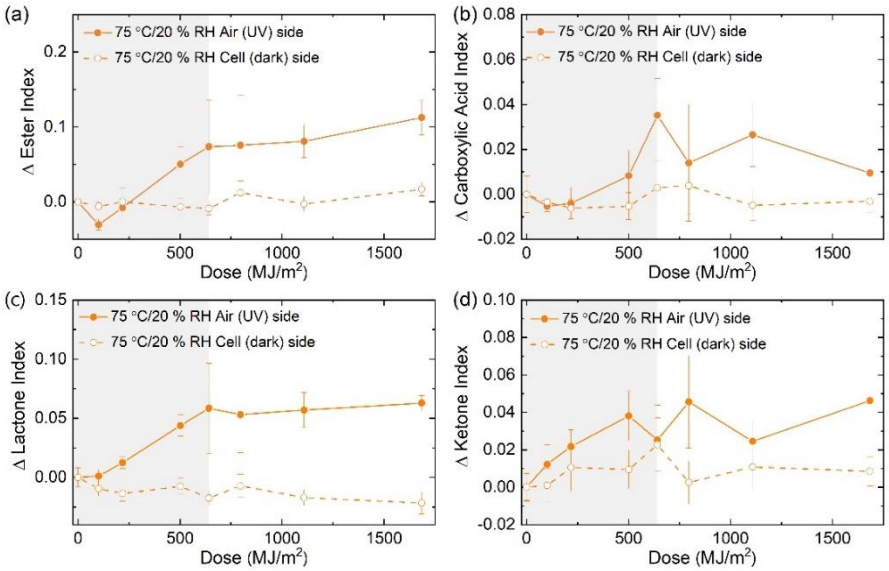

Fig. 4. (a) Ester index, (b) carboxylic acid index, (c) lactone index, and (d) ketone index of the air (UV) and cell (dark) side surfaces of PP-based backsheets over the course of artificial weathering at 75 °C/20 % RH, showing greater accumulation of carbonyl products on the air (UV) exposed side of the backsheets. Each data point represents an average of 3 measurements. Error bars show standard deviation. Graphs are shaded from 0 MJ/m^2 to 640 MJ/m^2. Points are connected to guide the eye.

3.2.3. Effect of environmental exposure conditions on carbonyl product formation

While some polymers are susceptible to accelerated degradation at higher humidities due to hydrolysis, PP is hydrophobic, and previous work has shown that PP is not prone to hydrolytic degradation in damp heat conditions for up to 3000 h exposure time [12]. A potential effect of humidity in PP degradation is slightly suppressed oxidation. Higher humidity in air results in slightly decreased partial pressure of oxygen (pO_2), resulting from the increased partial pressure of water vapor (pH_2O). Oxygen pressure is known to affect PP oxidation [70]. Additionally, chromophores are likely to be present on the films as a result of manufacture, even before exposure [36, 68]. Water molecules may form hydrogen bonds with these more polar species on the surface, hindering photo-oxidation.

The results of this experiment show the mean indices fall lower for higher humidity conditions than lower humidity conditions for nearly all points of comparison for esters and lactones, which is not observed for accumulation of carboxylic acids and ketones (Fig. 5). Of note is the apparent continuation of this trend after the saturation point has been reached. However, a significant effect cannot be concluded definitively based on the statistical analysis, due to the limited sample size and heterogeneous degradation. This remains an area for future inquiry.

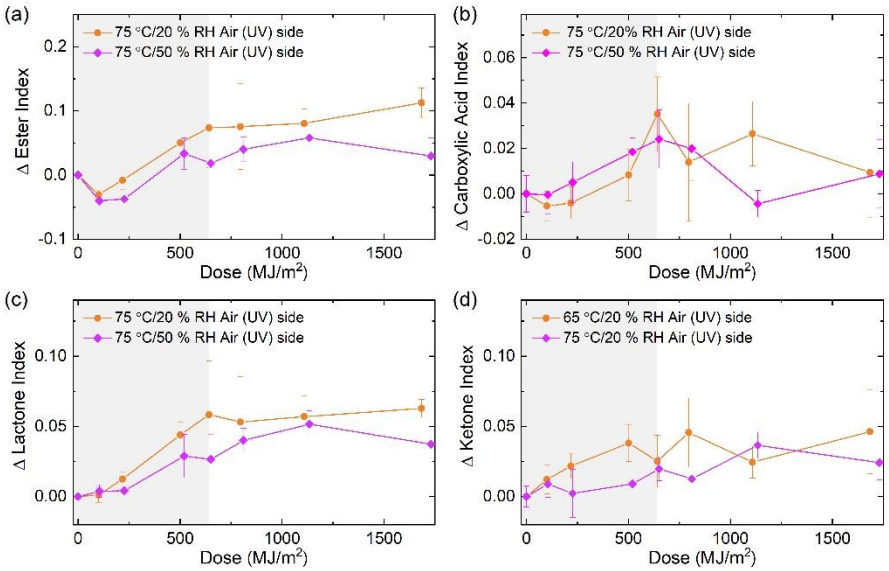

Fig. 5. (a) Ester index, (b) carboxylic acid index, (c) lactone index, and (d) ketone index of the air (UV) side surfaces of PP-based backsheets over the course of artificial weathering at 75 °C/20 % RH and 75 °C/50 % RH, showing a slight suppressive effect of higher humidity on ester and lactone accumulation. Indices are presented as change from initial value measured on unexposed backsheet. Each data point represents an average of 3 measurements. Error bars show standard deviation. Graphs are shaded from 0 MJ/m^2 to 640 MJ/m^2. Points are connected to guide the eye.

The results showed no significant effect of temperature on the product formation rates or quantities (Fig. 6), with the possible exception of vinyl and vinylidene, which showed increased average accumulation of both vinyl and vinylidene after the carbonyl products have reached stationary states in some measurement locations. The absence of a quantifiable temperature effect is likely due to the relatively small difference in temperature chosen for this experiment.

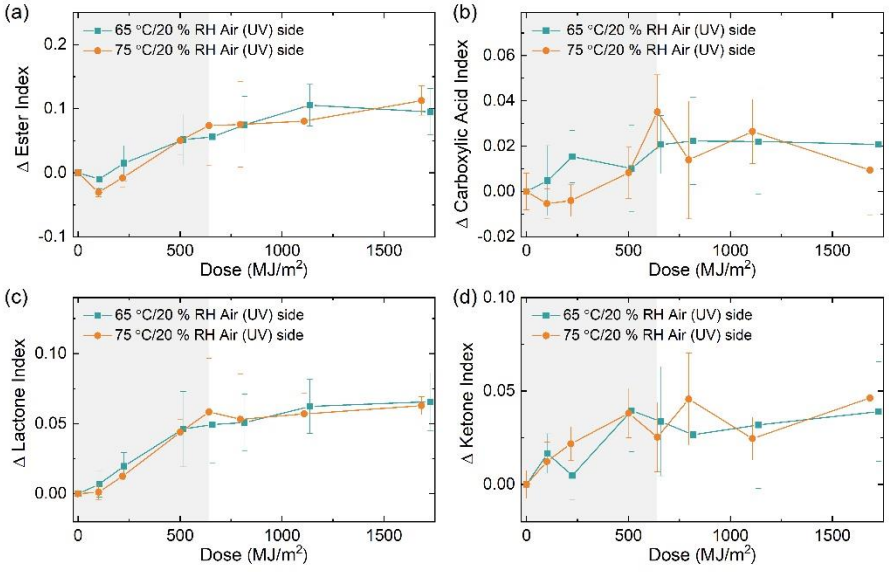

Fig. 6. (a) Ester index, (b) carboxylic acid index, (c) lactone index, and (d) ketone index of the air (UV) side surfaces of PP-based backsheets over the course of artificial weathering at 65 °C/20 % RH and 75 °C/20 % RH, showing no appreciable effect of temperature on oxidative product accumulation. Indices are presented as change from initial value measured on unexposed

backsheet. Each data point represents an average of 3 measurements. Error bars show standard deviation. Graphs are shaded from 0 MJ/m^2 to 640 MJ/m^2. Points are connected to guide the eye.

XPS analysis was employed to substantiate and elaborate upon observations of evolving surface characteristics of the PP backsheet samples over the course of exposure by examining the changing elemental composition. This analysis exposed the same general trends observed in FTIR quantification of carbonyl products. The C 1s spectrum of the PP surface was subjected to peak fitting to resolve separate peaks at approximately 285.5 eV, 286.8 eV, and 288.8 eV, which were attributed to C-C, C-O-C, and O-C=O, respectively. The 288.8 eV peak is of particular interest in this investigation, as it provides insight into carbonyl functional groups resulting from oxidative degradation. Over the course of exposure, the exposed side of the PP shows a relatively steep increase in the area of this peak in the early phase of the exposure, followed by a slow decrease (Fig. 7), which is mirrored in the behavior of the trends resulting from peak-resolving analysis of the FTIR results above for functional groups containing O-C=O bonds, such as esters, lactones, and acids (Fig. 4, Fig. 5, and Fig. 6).

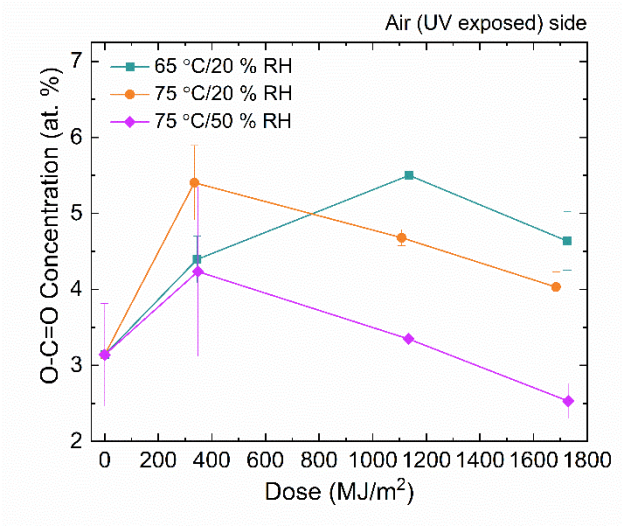

Fig. 7. Atomic percent (at. %) of C with bond configuration O-C=O measured on the air (UV-exposed) side of PP backsheets weathered at 65 °C/20 % RH, 75 °C/20 % RH, and 75 °C/50 % RH. Each data point represents an average of 3 measurements. Error bars show standard deviation. Points are connected to guide the eye.

3.2.4. Effect of environmental exposure conditions on vinyl and vinylidene formation

Vinyl and vinylidene products depend on the competition between formation and consumption of vinyl groups [31]. In the present study, these groups generally reach a relatively stable position early in the exposure, around 220 MJ/m^2, and show mostly small, fluctuating changes in value until approximately 1110 MJ/m^2 exposure, after the carbonyl products have reached a plateau (Fig. 8). Vinyl and vinylidene concentrations begin to rise again around 1110 MJ/m^2, though this behavior varies widely among the four sampling locations on each film, leading to greater uncertainty. The greatest influence on vinyl and vinylidene formation appears to be humidity, with higher humidity leading to lower concentrations over a portion of the exposure, likely due to decreased pO_2 as proposed above. Vinyl and vinylidene groups may enable crosslinking [32, 71], which may contribute to the slight embrittlement observed during fragmentation testing (Section 3.4.2).

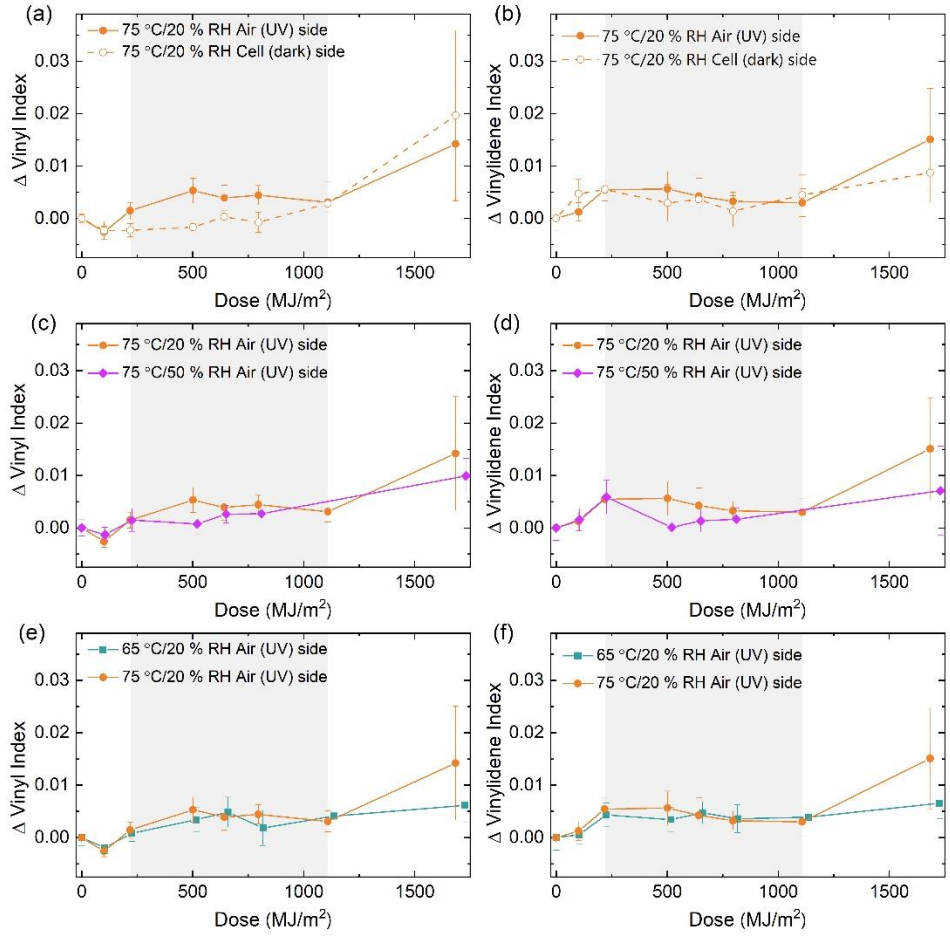

Fig. 8. Vinyl index and vinylidene index of the surfaces of PP-based backsheets over the course of artificial weathering: (a, b) Air (UV) and cell (dark) side of backsheets exposed at 75 °C/20 % RH; (c, d) Air (UV) side surfaces of PP-based backsheets exposed at 75 °C/20 % RH and 75 °C/50 % RH; (e, f) Air (UV) side surfaces of PP-based backsheets exposed at 65 °C/20 % RH and 75 °C/20 % RH. Each data point represents an average of 3 measurements. Error bars show standard deviation. Graphs are shaded from 220 MJ/m^2 to 1110 MJ/m^2. Points are connected to guide the eye.

3.2.5. Change in yellow index with exposure

Yellow index measurements typically serve as an indicator of chemical changes in the polymer structure. They are often a result of the accumulation of chromophores, which may arise from photo-oxidative degradation, which give a yellow appearance [1, 72]. In this investigation, all of the samples show extremely minor changes in yellowing over exposure of both the air and cell sides, with the exposed (air) side showing very closely grouped results for all three exposure conditions (Fig. 9). Towards the end of the exposure, a slight temperature effect is suggested, which is most prominent on the back (cell) side. Overall, the YI for all three samples deviate very little from the original values for unexposed films.

The back (cell) side results show more differentiation between the exposure conditions, with higher temperatures and higher humidities both leading to increased yellowing. These results suggest that bleaching could be contributing to the lack of yellowing observed on the exposed side; however, even on the back side, $\Delta YI \approx 0$ for films exposed at 65 °C/20 % RH and 75 °C/20 % RH, with only the backsheet exposed at 75 °C/50 % RH showing a quantifiable increase. Additionally, even this backsheet shows a change of only $\Delta YI < 1$. This result is in agreement with previous results on this material reporting

competition of very minor yellowing and photobleaching, resulting in nearly no net change in YI [26]. The dark (cell) side of the backsheets does show slightly higher concentrations of alkenes, which may contribute to the yellow color, and agrees with the YI results. However, the overall ΔYI remains very small, and the effect of exposure conditions on ΔYI is consequently very small as well.

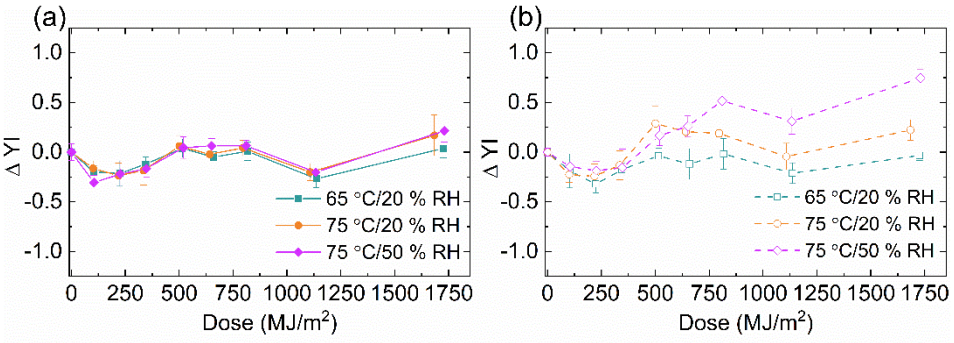

Fig. 9. Change in yellow index (ΔYI) of the (a) air (UV) and (b) cell (dark) side surfaces of PP-based backsheets over the course of artificial weathering at 65 °C/20 % RH, 75 °C/20 % RH, and 75 °C/50 % RH, showing greater yellowing on the cell side, as well as a significant effect of exposure conditions on yellow index on the back side. Each data point represents an average of 5 measurements. Error bars show standard deviation. Points are connected to guide the eye.

3.2.6. Implications for oxidative degradation pathways

Much of the photooxidation mechanism of PP is generally considered to be well-established [31-33, 69]. Degradation is considered to begin via radical initiation followed by propagation, generating a peroxide radical species [73-75]. These radicals may be primary, secondary, or tertiary radicals, which may in turn form primary, secondary, or tertiary peroxide radicals [74]. It should be noted that radical initiation is thought to be precipitated by initial impurities in the PP, likely initial thermal oxidation products from manufacture [31, 36]. This phenomenon may contribute to the preferential surface oxidation observed. The reactive peroxide radical can then abstract a labile hydrogen from another polymer molecule, generating hydroperoxide, the tertiary form of which is generally understood to be the main product resulting from radical initiation, and a key reactant in the subsequent steps of PP degradation. [69, 75]. Hydroperoxides may react to form alkoxyl radicals, which may be primary, secondary, or tertiary [74]. These alkoxyl radicals can abstract a hydrogen from the polymer chain and form corresponding alcohol species, which may undergo further oxidation, leading to alkenes, ketones, acids, and esters [74, 75]. Degradation of polypropylene is understood to primarily occur through *β*-scission of these alkoxyl radicals (Scheme 1) [32, 33, 75].

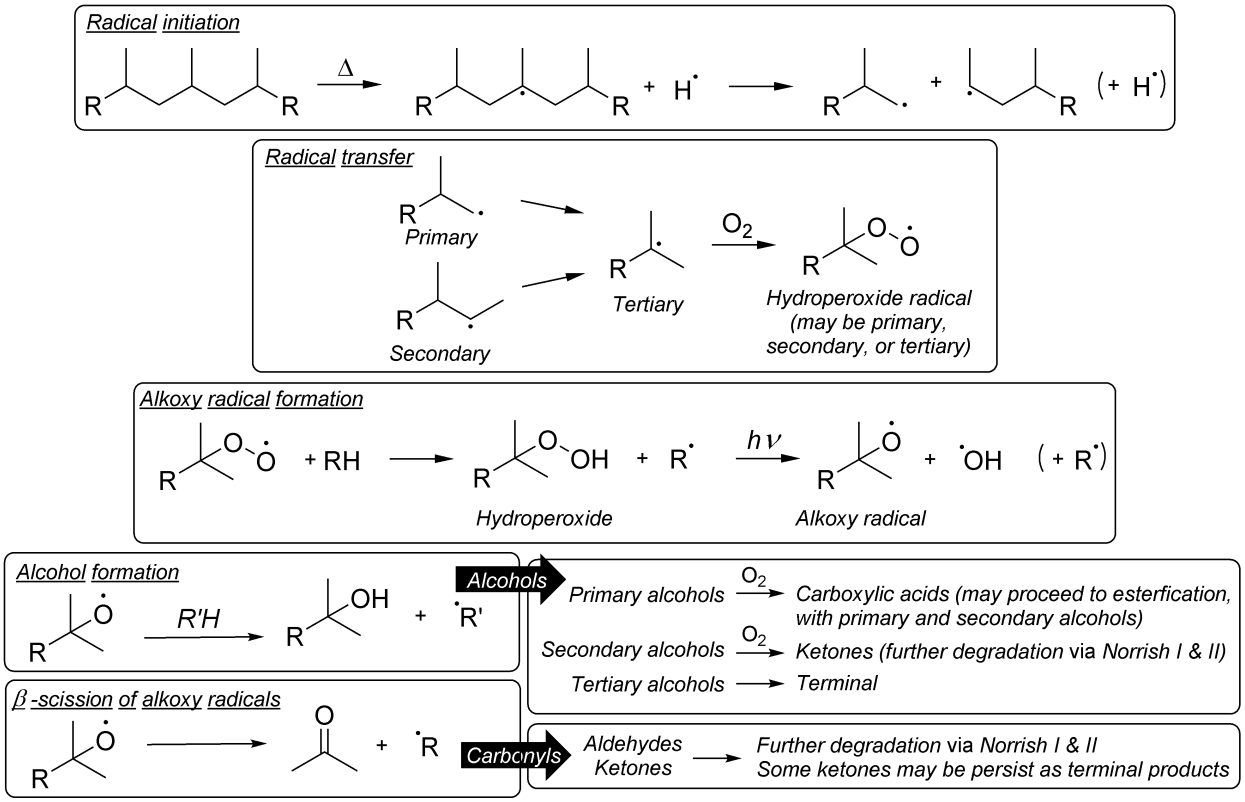

Scheme 1. Radical initiation and propagation and formation of hydroperoxides and alkoxy radicals.

Ketones formed by this mechanism may further decompose through the photochemical Norrish I and II reactions, (Scheme 2) producing a number of products, including alkenes such as vinyl and vinylidene, as well as carboxylic acids and ketones, which may go on to further react and form esters and other oxidation products [31].

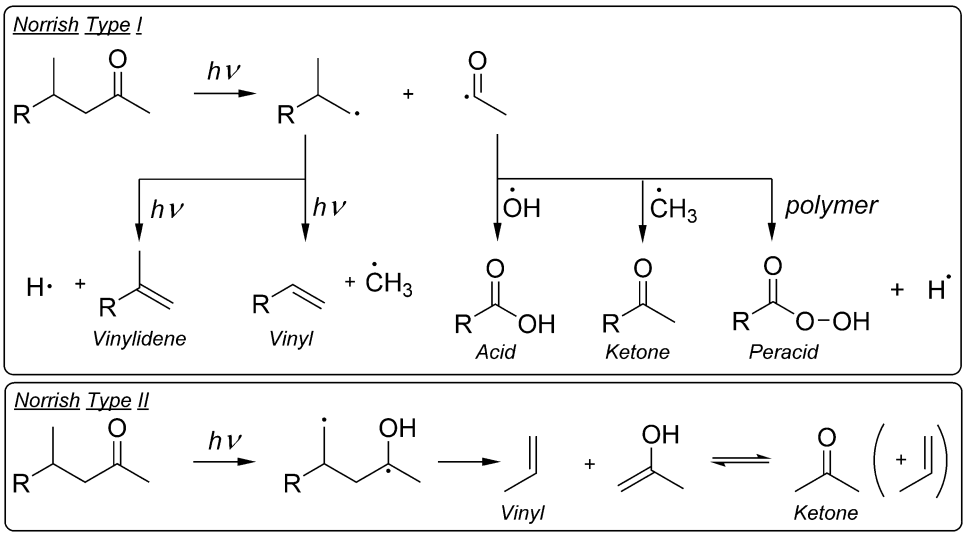

Scheme 2. Formation of oxidative degradation products of PP *via* Norrish Type I and II reactions.

In the present work, ester and lactone formation appears to have the most pronounced apparent dependence on weathering conditions, with the formation of lactones and esters only occurring under photo-oxidation (as opposed to acids and ketones, which still formed in small quantities on the unexposed surface, via thermally-driven oxidation) (Fig. 4). While several studies have asserted the presence of esters and lactones in photo-oxidized PP [28, 31, 32, 69], there are few which proposed or investigated a mechanism for such formation. One potential explanation for the disparity observed in this study is the possibility that the formation of these products is driven almost exclusively by the photolytic Norrish Type I reaction, which produces peracids, potential precursors to the formation of both lactones and esters (Scheme 2) [32]. Another proposes carboxylic acids and alcohol species formed via photooxidation undergo esterification with one another, a process which may be catalyzed by mineral fillers [74, 76]. It should be noted that the observed lactones in this study may form by way of intramolecular esterification in this manner, as well.

Geuskens and Kabamba proposed a mechanism for ester formation involving a photolysis of hydroperoxides and ketones [77]. This mechanism was supported in work by Philippart, *et al.*, who in turn observed an effect of light intensity on the distribution between acids and esters in photooxidized PP, showing that higher light intensity drives the decomposition of hydroperoxides towards esters [69]. Philippart *et al.* concluded that high ratios of light intensity and temperature affect the decomposition of hydroperoxides, with higher light intensity favoring esters and low molecular weight acids, and lower light intensity favoring "chain-end" acids formation [69]. The results presented here show a strong dependence on presence of UV irradiance for ester formation, but it should be emphasized that the present work does not examine variations of light intensity, and the observed ester and lactone disparity may be influenced by any of the factors discussed here.

Degradation pathways are of particular interest for the field of service life prediction for photovoltaics, as reciprocity is crucial to the reliability of accelerated weathering. For this reason, additional research may be necessary to elucidate the mechanism of acid and ester formation.

3.3. Observation of additive migration

Results for both sides of all backsheets show the emergence of a pair of sharp peaks 1577 cm^{-1} and 1543 cm^{-1} that are not associated with typical carbonyl degradation products (Fig. 10). The wavenumbers and shapes of the peaks suggest a carboxylate functional group. Calcium stearate ($CaSt_2$) is a carboxylate salt and known lubricant additive in PP manufacturing [34], with carboxylate bands occurring at 1577 cm^{-1} and 1543 cm^{-1}. The bands are associated with the antisymmetric stretching for unidentate and bidentate association with calcium ions [67]. Furthermore, XPS measurements of the cell side surfaces show surface accumulation of calcium over exposure which increases in a similar fashion to the FTIR carboxylate peaks (Fig. 12a). The identification of $CaSt_2$ is further supported by previous observations by Bak, *et al.* of migration behavior of $CaSt_2$ in PP composites under accelerated aging [34]. Therefore, this pair of peaks is concluded to be attributable to $CaSt_2$ migration in the backsheets.

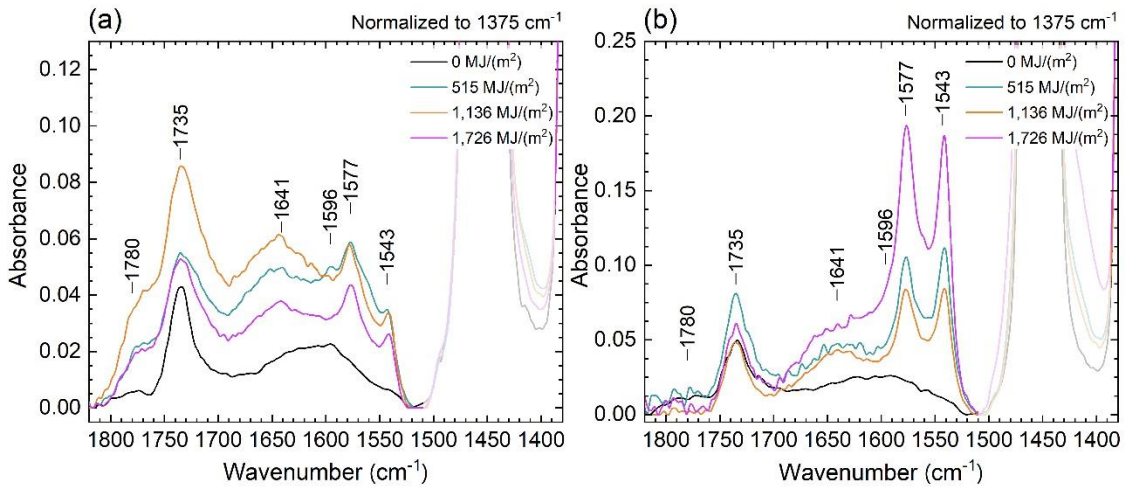

438

439 **Fig. 10.** Expansions (1820 cm^{-1} to 1380 cm^{-1}) of FTIR spectra of PP backsheets weathered at 65 °C/20 % RH, measured on the
440 (a) air (UV) side and (b) cell (dark) side, showing a pair of peaks at 1577 cm^{-1} and 1542 cm^{-1} attributed to $CaSt_2$ migration. Refer
441 to Figs. S8 and S9 for corresponding FTIR spectra of samples exposed at 75 °C/20 % RH and 75 °C/50 % RH.

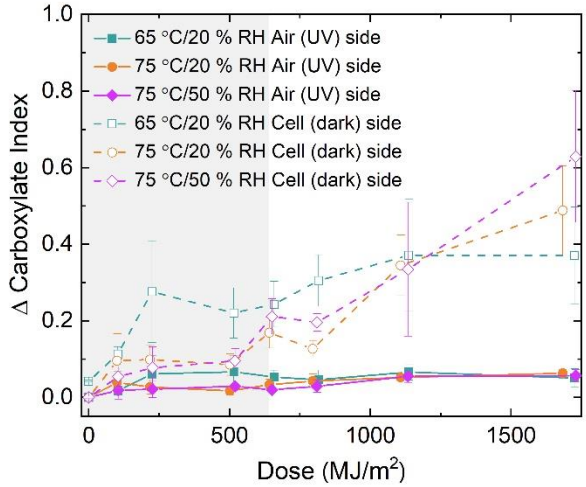

442

443 **Fig. 11.** Carboxylate index of the air (UV) and cell (dark) side surfaces of PP-based backsheets over the course of artificial
444 weathering at 65 °C/20 % RH, 75 °C/20 % RH, and 75 °C/50 % RH, showing increasing $CaSt_2$ migration to the cell (dark)
445 surface of the backsheets. Graph is shaded from 0 MJ/m^2 to 640 MJ/m^2. Each data point represents an average of 3
446 measurements. Error bars show standard deviation. Points are connected to guide the eye.

447 The $CaSt_2$ carboxylate peaks appear after initial exposure on both sides but show much greater
448 persistence on the cell side (dark side) (Fig. 11). On the cell side, these peaks continue to grow in
449 intensity throughout the exposure, even after the oxidative degradation products reach a saturation point.
450 However, FTIR peak behavior on the air side (UV-exposed side) suggests either unfavorable conditions
451 for migration of $CaSt_2$, or consistent removal of the substance through degradation or evaporation. The
452 carboxylate peaks reach a maximum intensity early in the exposure and remain much smaller than their
453 corresponding peaks on the cell side.

454 XPS results show calcium on both the exposed (air) side and dark (cell) side of the backsheets, with
455 calcium on the cell side increasing in concentration over exposure (Fig. 12a). Calcium on the air side

exceeds quantities found on the dark side, despite low prevalence of carboxylate peaks. This is likely due to multiple calcium sources, including both $CaSt_2$ and mineral fillers. Results of XPS quantification also showed continuous migration aluminum to the exposed surface (air side) (Fig. 12b). The calcium and aluminum observed on the air side of the backsheets are both attributable to mineral fillers commonly used in PP, such as talc and $CaCO_3$ [78]. Another possible contributor of aluminum is a Ziegler Natta catalyst, a polymerization catalyst used in PP production [79]. Of note is the observation that there is continuously increasing aluminum present on the air side, but no aluminum is observed on the cell side, suggesting a UV-driven migration mechanism.

Surface Raman measurements show an increase in intensity of TiO_2 peaks (450 cm^{-1} and 611 cm^{-1}) with exposure (Fig. S10 and Fig. S11) [62]. Figure S11 shows the increase in TiO_2 peak area over the course of exposure, with the greatest increase in peak area occurring in the first portion of exposure. This effect mirrors the trends of mineral additive accumulation on the backsheet seen in the XPS results, and it is further underscored by LSCM surface imaging showing surface residue accumulation in a similar pattern (see Section 3.4). This increased TiO_2 may be due to gradual loss of surface polymer, in addition to migration phenomena.

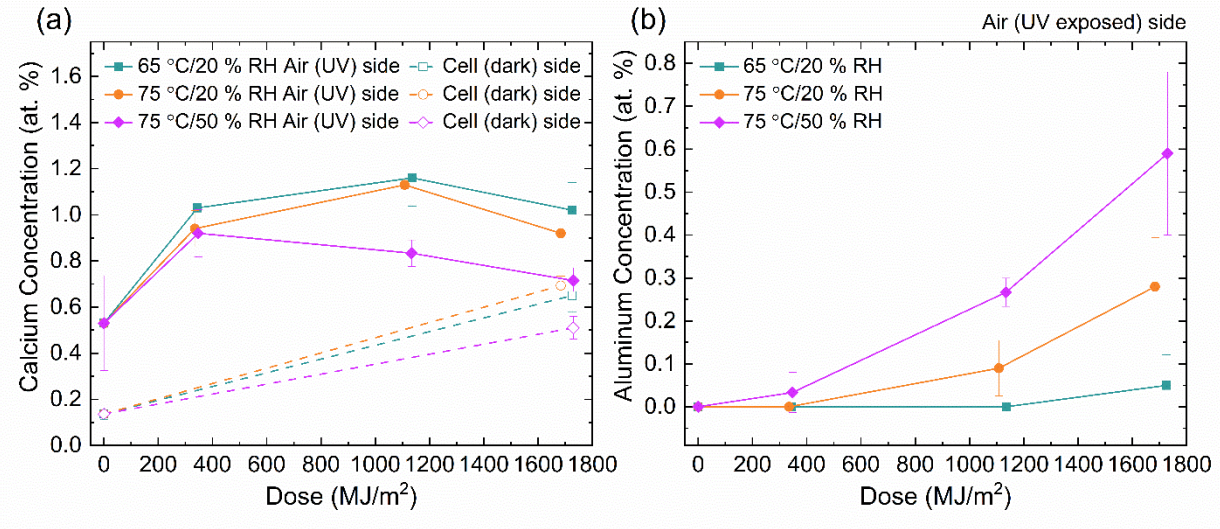

Fig. 12. Atomic percent (at. %) of calcium (a) and aluminum (b) measured on PP backsheets weathered at 65 °C/20 % RH, 75 °C/20 % RH, and 75 °C/50 % RH. Each data point represents an average of 3 measurements. Error bars show standard deviation. Points are connected to guide the eye.

3.4. Consequences of observed oxidation on material properties

The spectroscopic results presented have physical consequences on the durability of the films; notably, surface oxidation may correlate to eventual backsheet failure [18, 27]. Additionally, the formation of vinyl and vinylidenes may lead to crosslinking [32, 71], which is a potential contributor to embrittlement.

3.4.1. Surface morphology

LSCM measurement of the air (UV-exposed) side of the backsheets shows visible (Fig. 13) and quantifiable (Fig. S12) increases in surface roughness (measured as standard deviation of height, σ) after initial period of UV exposure, followed by surface erosion (Fig. S13). The UV dose at which the spike in roughness occurs varies across the films, but it consistently appears before 640 MJ/m^2, which is congruous with the observed change in oxidative product accumulation. Following this initial increase

and decrease in roughness, trends are more divergent, but generally show a much more gradual increase in surface roughness with increased exposure.

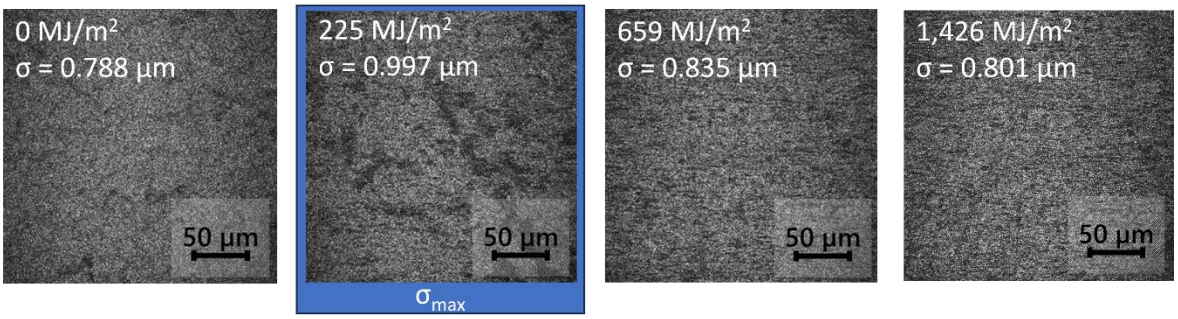

Fig. 13. 50x LSCM images of PP backsheet exposed to UV at 65 °C and 20 % RH after 0 MJ/m^2, 225 MJ/m^2, 659 MJ/m^2, and 1426 MJ/m^2 irradiance. Image size is 255 µm square, with 0.25 µm per pixel (xy).

Surface features appearing in the initial phase of exposure, such as minor pitting and small scratches, are observed in the LSCM images as gradually becoming less pronounced over the course of exposure, suggesting surface erosion over time (Fig. S13 and Fig. S14). However, a visible buildup is also detected in 5x LSCM images, tending to appear gradually in the latter half of exposure (Fig. S14). These are potentially the result of gradual PP loss with degradation, as seen in the FTIR results, leaving behind TiO_2 visible as chalking. Under greater magnification (50×), fragments of crystalline material are visible in small clusters on the surface of the sample (Fig. 14). This residue may be attributable to lingering salts associated with a polymerization catalyst from production (such as a Ziegler Natta catalyst) [79], to derivatives of such a catalyst, or to migration of mineral additives such as TiO_2 or $CaCO_3$. Any such identification would be supported by the surface presence of titanium and calcium observed in the XPS results. A combination of heterogeneous residue buildup and gradual surface erosion would account for the visible loss of topographic features in the polymer alongside the measured gradual increase in standard deviation of the surface height.

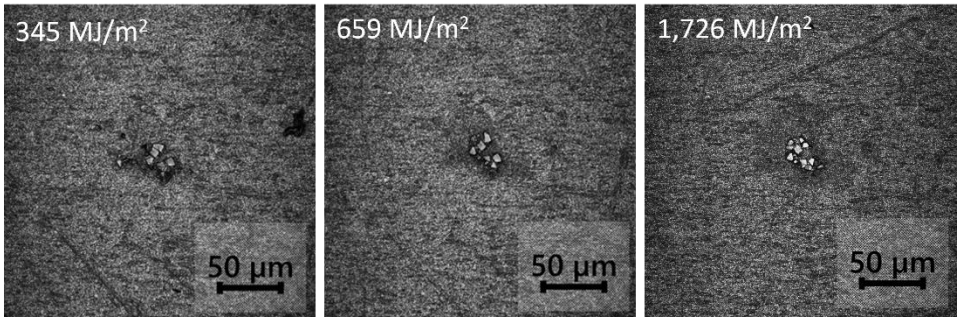

Fig. 14. 50x LSCM images of the same location on PP backsheet exposed to UV at 65 °C and 20 % RH after 345 MJ/m^2, 659 MJ/m^2, and 1726 MJ/m^2 irradiance. Image size is 255 µm square, with 0.25 µm per pixel (xy).

3.4.2. Fragmentation, crystallinity, and Young's modulus

To examine the degradation effect on crack propensity, samples were mounted on a mini tensile tester under a LSCM, and uniaxial strain was applied in increments. This method was previously shown to be capable of reproducing cracking in coextruded PA backsheets and laminated PPE backsheets, and allows for controlled, quantitative characterization of crack propensity [41]. Fig. 15 shows LSCM images of the aged PP backsheets after fragmentation testing, with fine, short, surface cracks visible at 20 % strain and above. This cracking may be attributed to embrittlement caused by the minor oxidative degradation

discussed above. The cracks observed do not show propagation across the sample, even at strains of 20 %. The line profile shown in Fig. 15c shows that these fine cracks are also confined fully to the outer layer of the backsheet, and generally do not exceed 3 µm in depth.

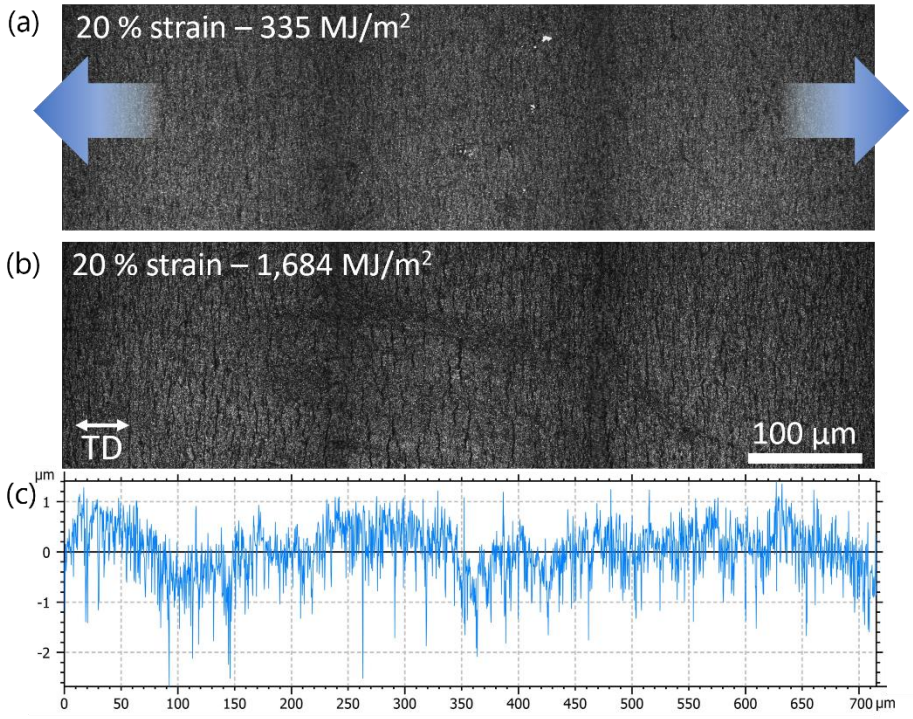

Fig. 15. LSCM images of fragmentation testing of PP backsheet after exposure to a) 335 MJ/m^2 and b) 1684 MJ/m^2 UV irradiance at 75 °C and 20 % RH. The sample was pulled in the transverse direction at a strain of 20 %. A line profile of a location on the same sample at 20 % strain, showing the cracks are < 3 µm deep.

Raman spectroscopy and nanoindentation were utilized to evaluate surface crystallinity and modulus of the PP backsheet air (UV-exposed) side. Crystallinity was calculated as the integrated area of the crystalline peak (810 cm^{-1}) [51, 54, 55] divided by the sum of the integrated areas of the crystalline peak, the isomeric defect phase peak (842 cm^{-1}), and the amorphous phase peak (830 cm^{-1}) [35, 51, 55]. The Raman spectra for these peaks can be seen in Fig. S15. The Raman results show a slight increase in crystallinity on the backsheets surface for all exposure conditions, with the greatest increase appearing in the first ≈340 MJ/m^2 of exposure, which is similar to the trends seen in other indicators of degradation (Fig. 16). Note that traditional differential scanning calorimetry (DSC), which measures the whole film, did not detect this superficial crystallinity change; utilizing Raman spectroscopy allows for greater sensitivity and enables surface-specific and depth-dependent crystallinity investigation [40]. Similarly, nanoindentation results show small increase in surface modulus following a similar trend. The results show little effect of exposure conditions on crystallinity and modulus change, suggesting the physical changes to be primarily due to UV oxidation. These changes of modulus and crystallinity account for the minor embrittlement of the PP backsheets that is apparent from the crack formation in the outer layer. However, the effect reaches a plateau after initial exposure and is relatively stable over the remainer of the exposure. As a result, the backsheets do not show signs of deep or propagating cracks even after high UV doses. The trend observed in these physical changes, including cracking, crystallinity, and modulus, all mirror the photooxidation trends observed in the chemical measurements described above.

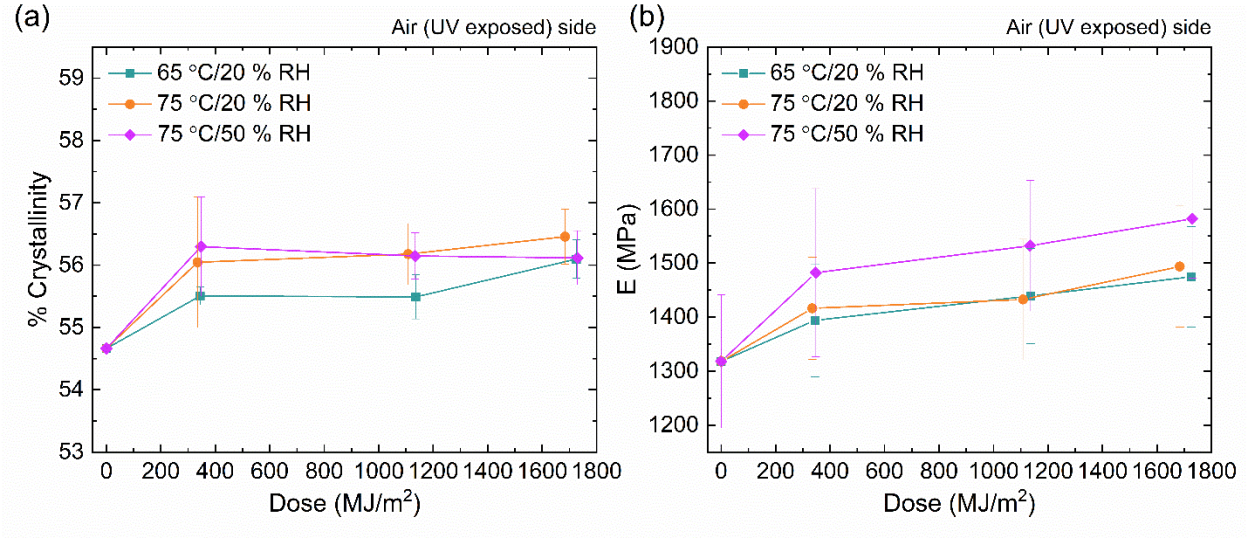

Fig. 16. (a) Change in crystallinity of PP backsheets as $A_{810}/(A_{830} + A_{842})$, obtained *via* surface Raman measurements, plotted vs. UV dose. (b) Change in surface modulus obtained *via* nanoindentation, plotted vs. UV dose. Trends show slight increase in crystallinity, with greatest increase in first ≈340 MJ/m^2 exposed. Each data point represents an average of 5 measurements. Error bars show standard deviation. Points are connected to guide the eye.

Previously, Oreski *et al.* performed aging utilizing sequential stress testing (UV exposure and thermo-mechanical load) on solder bump coupons with PP-based backsheets, finding that PP did not show crack initiation and propagation under these conditions [26]. While the present work did produce small cracks, it should be noted that these superficial cracks appeared under much greater strains than would be experienced in the field (10 % to 20 % experimental strains vs. < 5% field strain). Conversely, polyamide-based backsheets exposed to 735 MJ/m^2 UV at 65 °C/20 % RH, a much lower dose than achieved in the present study, showed deep crack formation extending through the outer layer and into the core layer (46.6 µm ± 2.0 µm) at only 4.5 % strain [41]. This highlights the potential of PP as a cracking-resistant backsheet alternative. Given the extreme conditions needed to produce even small cracks, and the failure of those cracks to propagate catastrophically, it's not likely the investigated backsheets would show cracking due to photo-oxidation in field modules.

4. Summary

Recently, research into fluoropolymer alternatives for PV backsheets has been driven by price pressure, the promise of improved performance, and concerns around sustainability and environmental responsibility. PP has emerged as a promising material for this application due to its low cost of production, availability, recyclability, and permeability, though work investigating the degradation of PP in PV backsheets remains limited. The aim of this work was to carefully examine the photooxidation of PP backsheets, formulated for use in PV installations and using test conditions informed by service conditions, providing a strong foundation for the continued expansion of the use of PP-based backsheets in the photovoltaic industry.

The backsheets showed minor decrease in intensity of characteristic PP peaks in the FTIR spectra for all exposure conditions, as well as minor accumulation of oxidation products. A thorough peak deconvolution process was applied to the FTIR region corresponding to oxidative products to obtain clear trends of oxidative products by functional group vs. exposure time under various conditions. All degradation products showed greater accumulation on the UV-exposed side, and the FTIR peak-resolving analysis of functional groups revealed a particular discrepancy in ester and lactone formation on the UV-

exposed (air) side vs. the dark (cell) side. Additionally, previously unassigned FTIR peaks corresponding to a known PP additive were identified and attributed to calcium stearate migration to the surface, with back (dark) side migration significantly exceeding that for the exposed (air) side.

To study the mechanical consequences of the oxidative degradation, crack propensity and crystallinity were examined, using fragmentation testing and Raman spectroscopy. Overall, all major markers of degradation, including oxidation product concentration, yellowing, fragmentation, and crystallinity, showed the greatest changes occurring in the initial phases of exposure. Over the full experiment, no properties examined showed signs of catastrophic degradation or failure, and fragmentation testing showed minor cracking extending only within the outer layer of the backsheet.

The present work elaborates on previous studies revealing the excellent stability of these emerging PP-based backsheets, including general resistance to oxidative degradation as well as mechanical failure. These results, together with existing work showing the desirable functional properties of this material, highlight the promise of PP-based backsheets as an inexpensive, recyclable, and durable alternative to fluoropolymer-based backsheets in PV modules.

Disclaimer

Certain commercial products or equipment are described in this article to adequately specify the procedure. In no case does such identification imply recommendation or endorsement by the National Institute of Standards and Technology, nor does it imply that it is necessarily the best available for the purpose.

REFERENCES

[1] M. Aghaei, A. Fairbrother, A. Gok, S. Ahmad, S. Kazim, K. Lobato, G. Oreski, A. Reinders, J. Schmitz, M. Theelen, P. Yilmaz, J. Kettle, Review of degradation and failure phenomena in photovoltaic modules, Renewable and Sustainable Energy Reviews 159 (2022) 112160. https://doi.org/10.1016/j.rser.2022.112160.

[2] A. Fairbrother, N. Phillips, X. Gu, 7 - Degradation Processes and Mechanisms of Backsheets, in: H.E. Yang, R.H. French, L.S. Bruckman (Eds.), Durability and Reliability of Polymers and Other Materials in Photovoltaic Modules, William Andrew Publishing2019, pp. 153-174. https://doi.org/10.1016/B978-0-12-811545-9.00007-0.

[3] N.G. Dhere, N.S. Shiradkar, E. Schneller, Device for detailed analysis of leakage current paths in photovoltaic modules under high voltage bias, Applied Physics Letters 104(11) (2014). https://doi.org/10.1063/1.4869028.

[4] M.C. Celina, Review of polymer oxidation and its relationship with materials performance and lifetime prediction, Polymer Degradation and Stability 98(12) (2013) 2419-2429. https://doi.org/10.1016/j.polymdegradstab.2013.06.024.

[5] R. Shivakumar, S.K. Tippabhotla, V.A. Handara, G. Illya, A.A.O. Tay, F. Novoa, R.H. Dauskardt, A.S. Budiman, Fracture Mechanics and Testing of Interface Adhesion Strength in Multilayered Structures – Application in Advanced Solar PV Materials and Technology, Procedia Engineering 139 (2016) 47-55. https://doi.org/10.1016/j.proeng.2015.09.232.

[6] P. Saxena, P. Shukla, A comparative analysis of the basic properties and applications of poly (vinylidene fluoride) (PVDF) and poly (methyl methacrylate) (PMMA), Polymer Bulletin 79(8) (2022) 5635-5665. https://doi.org/10.1007/s00289-021-03790-y.

[7] W. Gambogi, Y. Heta, K. Hashimoto, J. Kopchick, T. Felder, S. MacMaster, A. Bradley, B. Hamzavytehrany, L. Garreau-Iles, T. Aoki, K. Stika, T.J. Trout, T. Sample, A Comparison of Key PV Backsheet and Module Performance from Fielded Module Exposures and Accelerated Tests, IEEE Journal of Photovoltaics 4(3) (2014) 935-941. https://doi.org/10.1109/JPHOTOV.2014.2305472.

[8] S.L. Moffitt, P.-C. Pan, L. Perry, J. Tracy, K.R. Choudhury, M.D. Kempe, X. Gu, Microstructure changes during failure of PVDF-based photovoltaic backsheets, Progress in Photovoltaics: Research and Applications 31(1) (2023) 26-35. https://doi.org/10.1002/pip.3605.
[9] S. Uličná, R.L. Arnold, J.M. Newkirk, A. Sinha, K. Terwilliger, L.T. Schelhas, P. Pasmans, C. Thellen, D.C. Miller, Material characterization of seven photovoltaic backsheets using seven accelerated test conditions, Solar Energy Materials and Solar Cells 267 (2024) 112726. https://doi.org/10.1016/j.solmat.2024.112726.
[10] G. Oreski, A. Mihaljevic, Y. Voronko, G.C. Eder, Acetic acid permeation through photovoltaic backsheets: Influence of the composition on the permeation rate, Polymer Testing 60 (2017) 374-380. https://doi.org/10.1016/j.polymertesting.2017.04.025.
[11] G. Oreski, G.C. Eder, Y. Voronko, A. Omazic, L. Neumaier, W. Mühleisen, G. Ujvari, R. Ebner, M. Edler, Performance of PV modules using co-extruded backsheets based on polypropylene, Solar Energy Materials and Solar Cells 223 (2021) 110976. https://doi.org/10.1016/j.solmat.2021.110976.
[12] A. Omazic, G. Oreski, M. Edler, G.C. Eder, C. Hirschl, G. Pinter, M. Erceg, Increased reliability of modified polyolefin backsheet over commonly used polyester backsheets for crystalline PV modules, Journal of Applied Polymer Science 137(30) (2020) 48899. https://doi.org/10.1002/app.48899.
[13] J. Oh, B. Rammohan, A. Pavgi, S. Tatapudi, G. Tamizhmani, G. Kelly, M. Bolen, Reduction of PV Module Temperature Using Thermally Conductive Backsheets, IEEE Journal of Photovoltaics 8(5) (2018) 1160-1167. https://doi.org/10.1109/JPHOTOV.2018.2841511.
[14] S. Huber, M.K. Moe, N. Schmidbauer, G.H. Hansen, D. Herzke, Emissions from incineration of fluoropolymer materials. A literature survey, NILU OR (2009). https://nilu.com/publication/24739/
[15] N.R. Council, Sustainability and the U.S. EPA, The National Academies Press, Washington, DC, 2011. http://doi.org/10.17226/13152.
[16] P. de Wild, M. de Wild-Scholten, I. Goudswaard, Life cycle assessment of photovoltaic module backsheets, Progress in Photovoltaics: Research and Applications n/a(n/a). https://doi.org/10.1002/pip.3755.
[17] G.C. Eder, Y. Voronko, G. Oreski, W. Mühleisen, M. Knausz, A. Omazic, A. Rainer, C. Hirschl, H. Sonnleitner, Error analysis of aged modules with cracked polyamide backsheets, Solar Energy Materials and Solar Cells 203 (2019) 110194. https://doi.org/10.1016/j.solmat.2019.110194.
[18] Y. Lyu, J.H. Kim, A. Fairbrother, X. Gu, Degradation and Cracking Behavior of Polyamide-Based Backsheet Subjected to Sequential Fragmentation Test, IEEE Journal of Photovoltaics 8(6) (2018) 1748-1753. 10.1109/JPHOTOV.2018.2863789.
[19] M. Owen-Bellini, S.L. Moffitt, A. Sinha, A.M. Maes, J.J. Meert, T. Karin, C. Takacs, D.R. Jenket, J.Y. Hartley, D.C. Miller, P. Hacke, L.T. Schelhas, Towards validation of combined-accelerated stress testing through failure analysis of polyamide-based photovoltaic backsheets, Scientific Reports 11(1) (2021) 2019. https://doi.org/10.1038/s41598-021-81381-7.
[20] J. Pascual, M. García, J. Marcos, L. Marroyo, Analysis of polyamide and fluoropolymer backsheets: Degradation and insulation failure in field-aged photovoltaic modules, Progress in Photovoltaics: Research and Applications 31(5) (2023) 494-505. https://doi.org/10.1002/pip.3653.
[21] J. Tracy, W. Gambogi, T. Felder, L. Garreau-Iles, H. Hu, T.J. Trout, R. Khatri, X. Ji, Y. Heta, K.R. Choudhury, Survey of Material Degradation in Globally Fielded PV Modules, 2019 IEEE 46th Photovoltaic Specialists Conference (PVSC), 2019, pp. 0874-0879. https://doi.org/10.1109/PVSC40753.2019.8981140.
[22] M. Owen-Bellini, D.C. Miller, L.T. Schelhas, S.L. Moffitt, D.R. Jenket, A.M. Maes, J.Y. Hartley, T. Karin, P. Hacke, Correlation of advanced accelerated stress testing with polyamide-based photovoltaic backsheet field-failures, 2019 IEEE 46th Photovoltaic Specialists Conference (PVSC), 2019, pp. 1995-1999. https://doi.org/10.1109/PVSC40753.2019.8980750.
[23] P. Hacke, M. Owen-Bellini, M. Kempe, D.C. Miller, T. Tanahashi, K. Sakurai, W.J. Gambogi, J.T. Trout, T.C. Felder, K.R. Choudhury, N.H. Philips, M. Koehl, K.-A. Weiss, S. Spataru, C. Monokroussos, G. Mathiak, 11 - Combined and Sequential Accelerated Stress Testing for Derisking Photovoltaic

Modules, in: D. Ginley, T. Fix (Eds.), Advanced Micro- and Nanomaterials for Photovoltaics, Elsevier2019, pp. 279-313. https://doi.org/10.1016/B978-0-12-814501-2.00011-6.
[24] W. Gambogi, B.L. Yu, T. Felder, S. MacMaster, K.R. Choudhury, J. Tracy, N. Phillips, H. Hu, Development of Accelerated Test Sequences to Assess Long Term Durability of PV Modules, 2019 IEEE 46th Photovoltaic Specialists Conference (PVSC), 2019, pp. 2406-2410. https://doi.org/10.1109/PVSC40753.2019.8981222.
[25] M.D. Kempe, T. Lockman, J. Morse, Development of Testing Methods to Predict Cracking in Photovoltaic Backsheets, 2019 IEEE 46th Photovoltaic Specialists Conference (PVSC), 2019, pp. 2411-2416. https://doi.org/10.1109/PVSC40753.2019.8980818.
[26] G. Oreski, C. Barretta, A. Macher, G. Eder, L. Neumaier, M. Feichtner, M. Aarnio-Winterhof, Investigation of the crack propensity of co-extruded polypropylene backsheet films for photovoltaic modules, Solar Energy Materials and Solar Cells 259 (2023) 112438. https://doi.org/10.1016/j.solmat.2023.112438.
[27] M. Thuis, N.M.A. Hasan, R.L. Arnold, B. King, A. Maes, D.C. Miller, J.M. Newkirk, L.T. Schelhas, A. Sinha, K. Terwilliger, S. Uličná, K.V. Durme, A Comparison of Emerging Nonfluoropolymer-Based Coextruded PV Backsheets to Industry-Benchmark Technologies, IEEE Journal of Photovoltaics 12(1) (2022) 88-96. https://doi.org/10.1109/JPHOTOV.2021.3117915.
[28] S. Aslanzadeh, M. Haghighat Kish, Photo-oxidation of polypropylene fibers exposed to short wavelength UV radiations, Fibers and Polymers 11(5) (2010) 710-718. https://doi.org/10.1007/s12221-010-0710-8.
[29] M. Bertoldo, S. Bronco, C. Cappelli, T. Gragnoli, L. Andreotti, Combining Theory and Experiment to Study the Photooxidation of Polyethylene and Polypropylene, The Journal of Physical Chemistry B 107(43) (2003) 11880-11888. https://doi.org/10.1021/jp035427h.
[30] C.L. de Carvalho, A.F. Silveira, D.d.S. Rosa, A study of the controlled degradation of polypropylene containing pro-oxidant agents, SpringerPlus 2(1) (2013) 623. https://doi.org/10.1186/2193-1801-2-623.
[31] Y. Lv, Y. Huang, J. Yang, M. Kong, H. Yang, J. Zhao, G. Li, Outdoor and accelerated laboratory weathering of polypropylene: A comparison and correlation study, Polymer Degradation and Stability 112 (2015) 145-159. https://doi.org/10.1016/j.polymdegradstab.2014.12.023.
[32] K. Rajakumar, V. Sarasvathy, A. Thamarai Chelvan, R. Chitra, C.T. Vijayakumar, Natural Weathering Studies of Polypropylene, Journal of Polymers and the Environment 17(3) (2009) 191-202. https://doi.org/10.1007/s10924-009-0138-7.
[33] F. Severini, R. Gallo, S. Ipsale, Environmental degradation of polypropylene, Polymer Degradation and Stability 22(2) (1988) 185-194. https://doi.org/10.1016/0141-3910(88)90041-9.
[34] M.-G. Bak, J.-S. Won, S.-W. Koo, A. Oh, H.-K. Lee, D.-S. Kim, S.-G. Lee, Migration Behavior of Lubricants in Polypropylene Composites under Accelerated Thermal Aging, Polymers, 2021. https://doi.org/10.3390/polym13111723.
[35] M.S. Rabello, J.R. White, The role of physical structure and morphology in the photodegradation behaviour of polypropylene, Polymer Degradation and Stability 56(1) (1997) 55-73. https://doi.org/10.1016/S0141-3910(96)00202-9.
[36] D.J. Carlsson, D.M. Wiles, Photooxidation of Polypropylene Films. IV. Surface Changes Studied by Attenuated Total Reflection Spectroscopy, Macromolecules 4(2) (1971) 174-179. 10.1021/ma60020a008.
[37] Y. Lyu, A. Fairbrother, J.H. Kim, M. Gong, L.-P. Sung, S.S. Watson, X. Gu, Fluorescence imaging analysis of depth-dependent degradation in photovoltaic laminates: insights to the failure, Progress in Photovoltaics: Research and Applications 28(2) (2020) 122-134. https://doi.org/10.1002/pip.3212.
[38] C.-C. Lin, P.J. Krommenhoek, S.S. Watson, X. Gu, Depth profiling of degradation of multilayer photovoltaic backsheets after accelerated laboratory weathering: Cross-sectional Raman imaging, Solar Energy Materials and Solar Cells 144 (2016) 289-299. https://doi.org/10.1016/j.solmat.2015.09.021.
[39] B. Mailhot, P.-O. Bussière, A. Rivaton, S. Morlat-Thérias, J.-L. Gardette, Depth Profiling by AFM Nanoindentations and Micro-FTIR Spectroscopy for the Study of Polymer Ageing, Macromolecular Rapid Communications 25(2) (2004) 436-440. https://doi.org/10.1002/marc.200300110.

[40] A. Aiello, S. Mitterhofer, J. Obrzut, K. Jensen, P. Wasik, C. Barretta, G. Oreski, S.S. Watson, L. Sung, X. Gu, A Spatially-Resolved Evaluation of Accelerated Environmental Aging on Emerging Polypropylene-based Photovoltaic Backsheets using Raman Spectroscopy, NIST Engineering Laboratory, 2024.
[41] S. Mitterhofer, M. Kempe, X. Gu, Evaluation of Surface Crack Formation in Photovoltaic Backsheets Using Fragmentation and Finite Element Simulations, IEEE Journal of Photovoltaics 14(2) (2024). https://doi.org/10.1109/JPHOTOV.2024.3356119.
[42] J. Chin, E. Byrd, N. Embree, J. Garver, B. Dickens, T. Finn, J. Martin, Accelerated UV weathering device based on integrating sphere technology, Review of Scientific Instruments 75(11) (2004) 4951-4959. https://doi.org/10.1063/1.1808916.
[43] T. Barnes, DuraMAT FY 2023 Annual Report: Toward Reliability Forecasting, United States, 2024. https://www.osti.gov/biblio/2319198

https://www.osti.gov/servlets/purl/2319198
[44] IEC, Measurement procedures for materials used in photovoltaic modules - Part 2: Polymeric materials - Frontsheets and backsheets, IEC TS 62788-2, 2024, p. 94. https://webstore.iec.ch/en/publication/66171
[45] P. Bruździak, Vapor correction of FTIR spectra – A simple automatic least squares approach, Spectrochimica Acta Part A: Molecular and Biomolecular Spectroscopy 223 (2019) 117373. https://doi.org/10.1016/j.saa.2019.117373.
[46] Origin(Pro), OriginLab Corporation, Northampton, MA, United States, 2020.
[47] ZEN (Lite), Carl Zeiss Microscopy GmbH, Jena, Germany, 2023.
[48] ConfoMap ST, Carl Zeiss Microscopy, Jena, Germany, 2017.
[49] X. Li, B. Bhushan, A review of nanoindentation continuous stiffness measurement technique and its applications, Materials Characterization 48(1) (2002) 11-36. https://doi.org/10.1016/S1044-5803(02)00192-4.
[50] S. Mitterhofer, S. Smith, A. Aiello, K. Jensen, X. Gu, Spatially resolved modulus measurements of photovoltaic encapsulation materials using cross-sectional nano-indentation, NIST Engineering Laboratory (2024).
[51] R. Chércoles Asensio, M. San Andrés Moya, J.M. de la Roja, M. Gómez, Analytical characterization of polymers used in conservation and restoration by ATR-FTIR spectroscopy, Analytical and Bioanalytical Chemistry 395(7) (2009) 2081-2096. https://doi.org/10.1007/s00216-009-3201-2.
[52] B.C. Smith, The Infrared Spectroscopy of Polymers II: Polyethylene, Spectroscopy 36(9) (2021) 24-29. https://doi.org/10.56530/spectroscopy.xp7081p7.
[53] B.C. Smith, The Infrared Spectra of Polymers III: Hydrocarbon Polymers, Spectroscopy 36(11) (2021) 22-25. https://doi.org/10.56530/spectroscopy.mh7872q7.
[54] M. Arruebarrena de Báez, P.J. Hendra, M. Judkins, The Raman spectra of oriented isotactic polypropylene, Spectrochimica Acta Part A: Molecular and Biomolecular Spectroscopy 51(12) (1995) 2117-2124. https://doi.org/10.1016/0584-8539(95)01512-1.
[55] A.S. Nielsen, D.N. Batchelder, R. Pyrz, Estimation of crystallinity of isotactic polypropylene using Raman spectroscopy, Polymer 43(9) (2002) 2671-2676. https://doi.org/10.1016/S0032-3861(02)00053-8.
[56] A. Gopanna, R.N. Mandapati, S.P. Thomas, K. Rajan, M. Chavali, Fourier transform infrared spectroscopy (FTIR), Raman spectroscopy and wide-angle X-ray scattering (WAXS) of polypropylene (PP)/cyclic olefin copolymer (COC) blends for qualitative and quantitative analysis, Polymer Bulletin 76(8) (2019) 4259-4274. https://doi.org/10.1007/s00289-018-2599-0.
[57] M. Peltzer, C. Simoneau, Report of an interlaboratory comparison from the European Reference Laboratory for Food Contact : ILC002 2013 - Identification of polymeric materials, Luxembourg, 2013. https://doi.org/10.2788/6233.
[58] S. Abbate, G. Zerbi, S.L. Wunder, Fermi resonances and vibrational spectra of crystalline and amorphous polyethylene chains, The Journal of Physical Chemistry 86(16) (1982) 3140-3149. https://doi.org/10.1021/j100213a017.

[59] C.C. Naylor, R.J. Meier, B.J. Kip, K.P.J. Williams, S.M. Mason, N. Conroy, D.L. Gerrard, Raman Spectroscopy Employed for the Determination of the Intermediate Phase in Polyethylene, Macromolecules 28(8) (1995) 2969-2978. https://doi.org/10.1021/ma00112a050.
[60] T. Furukawa, H. Sato, Y. Kita, K. Matsukawa, H. Yamaguchi, S. Ochiai, H.W. Siesler, Y. Ozaki, Molecular Structure, Crystallinity and Morphology of Polyethylene/Polypropylene Blends Studied by Raman Mapping, Scanning Electron Microscopy, Wide Angle X-Ray Diffraction, and Differential Scanning Calorimetry, Polymer Journal 38 (2006) 1127-1136. https://doi.org/10.1295/polymj.PJ2006056.
[61] F.J. Lanyi, N. Wenzke, J. Kaschta, D.W. Schubert, A method to reveal bulk and surface crystallinity of Polypropylene by FTIR spectroscopy - Suitable for fibers and nonwovens, Polymer Testing 71 (2018) 49-55. https://doi.org/10.1016/j.polymertesting.2018.08.018.
[62] W. Bahloul, F. Mélis, V. Bounor-Legaré, P. Cassagnau, Structural characterisation and antibacterial activity of PP/TiO2 nanocomposites prepared by an in situ sol–gel method, Materials Chemistry and Physics 134(1) (2012) 399-406. https://doi.org/10.1016/j.matchemphys.2012.03.008.
[63] U. Balachandran, N.G. Eror, Raman spectra of titanium dioxide, Journal of Solid State Chemistry 42(3) (1982) 276-282. https://doi.org/10.1016/0022-4596(82)90006-8.
[64] B.C. Smith, Infrared Spectral Interpretation: A Systematic Approach, CRC Press, LLC1999. https://www.routledge.com/Infrared-Spectral-Interpretation-A-Systematic-Approach/Smith/p/book/9780849324635
[65] Q. Wu, B. Qu, Y. Xu, Q. Wu, Surface photo-oxidation and photostabilization of photocross-linked polyethylene, Polymer Degradation and Stability 68(1) (2000) 97-102. https://doi.org/10.1016/S0141-3910(99)00171-8.
[66] X.u. Zhao, Z. Li, Y. Chen, L. Shi, Y. Zhu, Solid-phase photocatalytic degradation of polyethylene plastic under UV and solar light irradiation, Journal of Molecular Catalysis A: Chemical 268(1) (2007) 101-106. https://doi.org/10.1016/j.molcata.2006.12.012.
[67] M. Gönen, S. Öztürk, D. Balköse, S. Okur, S. Ülkü, Preparation and Characterization of Calcium Stearate Powders and Films Prepared by Precipitation and Langmuir−Blodgett Techniques, Industrial & Engineering Chemistry Research 49(4) (2010) 1732-1736. https://doi.org/10.1021/ie901437d.
[68] D.J. Carlsson, D.M. Wiles, Photooxidation of Polypropylene Films. V. Origin of Preferential Surface Oxidation, Macromolecules 4(2) (1971) 179-184. 10.1021/ma60020a009.
[69] J.-L. Philippart, C. Sinturel, R. Arnaud, J.-L. Gardette, Influence of the exposure parameters on the mechanism of photooxidation of polypropylene, Polymer Degradation and Stability 64(2) (1999) 213-225. https://doi.org/10.1016/S0141-3910(98)00191-8.
[70] E. Richaud, F. Farcas, P. Bartoloméo, B. Fayolle, L. Audouin, J. Verdu, Effect of oxygen pressure on the oxidation kinetics of unstabilised polypropylene, Polymer Degradation and Stability 91(2) (2006) 398-405. https://doi.org/10.1016/j.polymdegradstab.2005.04.043.
[71] K. Liu, D.C. Miller, N. Bosco, R.H. Dauskardt, Determining the Crosslinking and Degradation Reaction Kinetics in Photovoltaic Encapsulants Using Accelerated Aging: Preprint, 52nd IEEE Photovoltaic Specialists Conference (PVSC52), 9-14 June 2024, Seattle, Washington, United States, 2024. https://www.nrel.gov/docs/fy24osti/90303.pdf
[72] F. Liu, L. Jiang, S. Yang, Ultra-violet degradation behavior of polymeric backsheets for photovoltaic modules, Solar Energy 108 (2014) 88-100. https://doi.org/10.1016/j.solener.2014.06.027.
[73] J.D. Peterson, S. Vyazovkin, C.A. Wight, Kinetics of the Thermal and Thermo-Oxidative Degradation of Polystyrene, Polyethylene and Poly(propylene), Macromolecular Chemistry and Physics 202(6) (2001) 775-784. https://doi.org/10.1002/1521-3935(20010301)202:6<775::AID-MACP775>3.0.CO;2-G.
[74] L.T. Saw, D.N. Uy Lan, N.A.A. Rahim, A.W. Mohd Kahar, C.X. Viet, Processing degradation of polypropylene-ethylene copolymer-kaolin composites by a twin-screw extruder, Polymer Degradation and Stability 111 (2015) 32-37. https://doi.org/10.1016/j.polymdegradstab.2014.10.024.
[75] J. Lacoste, D. Vaillant, D.J. Carlsson, Gamma-, photo-, and thermally-initiated oxidation of isotactic polypropylene, Journal of Polymer Science Part A: Polymer Chemistry 31(3) (1993) 715-722. https://doi.org/10.1002/pola.1993.080310316.

[76] F. Gugumus, Formation of ester functional groups in oxidizing polymers, Polymer Degradation and Stability 65(1) (1999) 5-13. https://doi.org/10.1016/S0141-3910(98)00208-0.
[77] G. Geuskens, M.S. Kabamba, Photo-oxidation of polymers—Part V: A new chain scission mechanism in polyolefins, Polymer Degradation and Stability 4(1) (1982) 69-76. https://doi.org/10.1016/0141-3910(82)90007-6.
[78] N.S. Yousef, Statistical Study on Additives Used to Improve Mechanical Properties of Polypropylene, Polymers (Basel) 14(1) (2022). https://doi.org/10.3390/polym14010179.
[79] I. Blakey, G.A. George, Raman spectral mapping of photo-oxidised polypropylene, Polymer Degradation and Stability 70(2) (2000) 269-275. https://doi.org/10.1016/S0141-3910(00)00126-9.